Available online at www.sciencedirect.com
SCIENCE DIRECT
Cement and Concrete Research 36 (2006) 761 – 775
Cement and Concrete Research

Non-structural cracking in RC walls: Part II. Quantitative prediction model

Hyo-Gyoung Kwak *, Soo-Jun Ha

Department of Civil and Environmental Engineering, Korea Advanced Institute of Science and Technology, Daejeon 305-701, South Korea

Received 17 October 2005; accepted 6 December 2005

Abstract

In this paper, for a quantitative assessment of non-structural cracking in an RC wall, an improved analytical model is proposed. First of all, to quantitatively calculate the cracking potential, an analytical model that can estimate the post-cracking behavior in an RC tension member is proposed. Unlike conventional approaches that use the bond–slip relationship or the assumed bond stress distribution, in our proposed approach the tensile strength of concrete at the post-cracking stage is quantified on the basis of polynomial strain distribution functions of steel and concrete. Predictions of cracking loads and elongations of reinforcing steel in RC tension members using the proposed model show good agreement with results from previous analytical studies and from experimental data. Subsequent comparisons of analytical results with test results verify that the combined use of both the approach in this paper as well as the approach previously introduced in the companion paper to this research make it possible to accurately predict the cracking behavior of RC walls. Additionally, the influence of changes in the material properties and construction conditions on the cracking in RC walls is investigated theoretically, using the numerical model proposed in this paper.

Keywords: Modeling; Tension stiffening; Temperature; Humidity; Concrete

1. Introduction

Non-structural cracks frequently occur either on the surface or through the depth in concrete structures. These cracks accelerate corrosion of the embedded reinforcing steel and lead to deterioration of the concrete. Since these cracks shorten the service life and increase the maintenance costs of concrete structures, minimizing these cracks is essential. In reinforced concrete (RC) wall structures under construction, cracks usually occur due to the restraint of volume change induced by shrinkage and hydration heat. Since the bottom face of wall structures is restrained by the foundation, tensile stresses develop along the restraint direction and cracks form perpendicular to the restraint at uniform intervals along the structure when the tensile stress is greater than the tensile strength of concrete at an arbitrary time t_n.

To estimate volume change cracking in RC walls, many crack spacing and width-predicting formulas have been proposed [1–4]. In particular, Rawi et al. [4] carried out important experimental works to study cracking due to the volume change of RC walls and suggested a formula based on the experimental data. In spite of extensive research and the proposal of numerous formulas, several problems remain in the prediction of non-structural cracking behavior of RC walls. For example, the formula proposed by Hughes [1] cannot detect the variation of crack width with height, the formula proposed by Stoffers [2] does not consider the effect of reinforcement in calculating crack spacing. Additionally, most of the previously proposed formulas [1–3] cannot predict the occurrence of a secondary crack or its propagation height. Moreover, all the previous numerical models [1–4] imperfectly predict the cracking behavior of RC walls because the models are based on assumptions of average volume change and full restraint of the bottom face of walls. Accordingly, to overcome these shortcomings for an accurate prediction of the cracking behavior in RC walls, an improved analytical approach that can determine crack spaces and widths on the basis of polynomial strain distribution functions of steel and concrete is introduced in this paper.

In a cracked cross-section, all tensile forces are balanced only by the steel encased in the concrete matrix. However,

* Corresponding author. Tel.: +82 42 869 3621; fax: +82 42 869 3610.
E-mail address: khg@kaist.ac.kr (H.-G. Kwak).

0008-8846/$ - see front matter © 2005 Elsevier Ltd. All rights reserved.
doi:10.1016/j.cemconres.2005.12.002

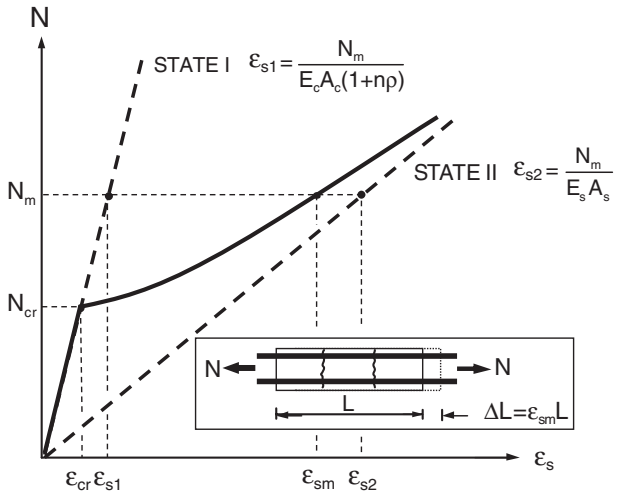

Fig. 1. Tensile force versus strain diagram.

between adjacent cracks, tensile forces are transmitted from the steel to the surrounding concrete by bond forces. This effect is called the tension stiffening effect. As shown in Fig. 1, a partially cracked RC member represents the structural response located in a region bounded by the two limit states of the uncracked and fully cracked states. Several methods have been used to determine the stiffening effect of the concrete between cracks. These can be broadly classified into two types of approach. The first, as adopted in the CEB-FIP Code [5], is based on the average strain in the member. The second, as adopted in the ACI 224 [6], uses the effective area of concrete, which is similar to the effective moment of inertia concept for the evaluation of deflections [7].

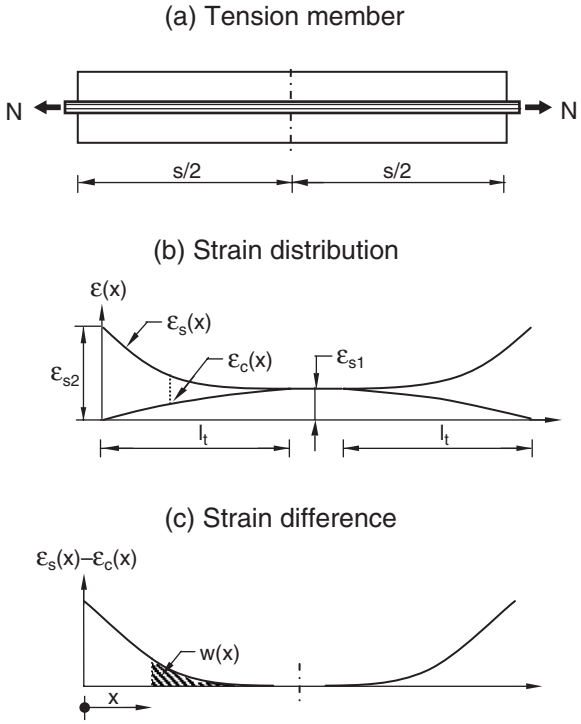

Fig. 2. Behavior of tension member.

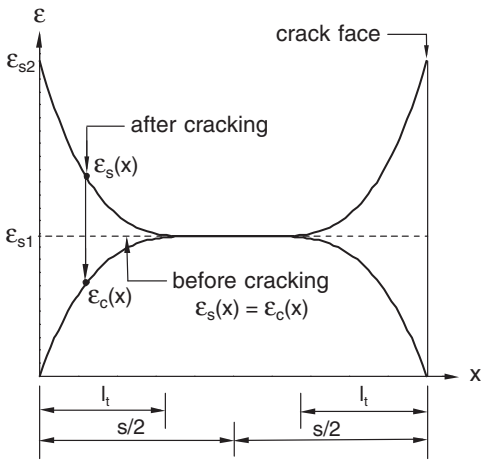

Fig. 3. Strain distribution after cracking.

Recently, with the increased use of the modified compression field theory (MCFT) [8] and softened truss model theory (STMT) [9], both of which employ average

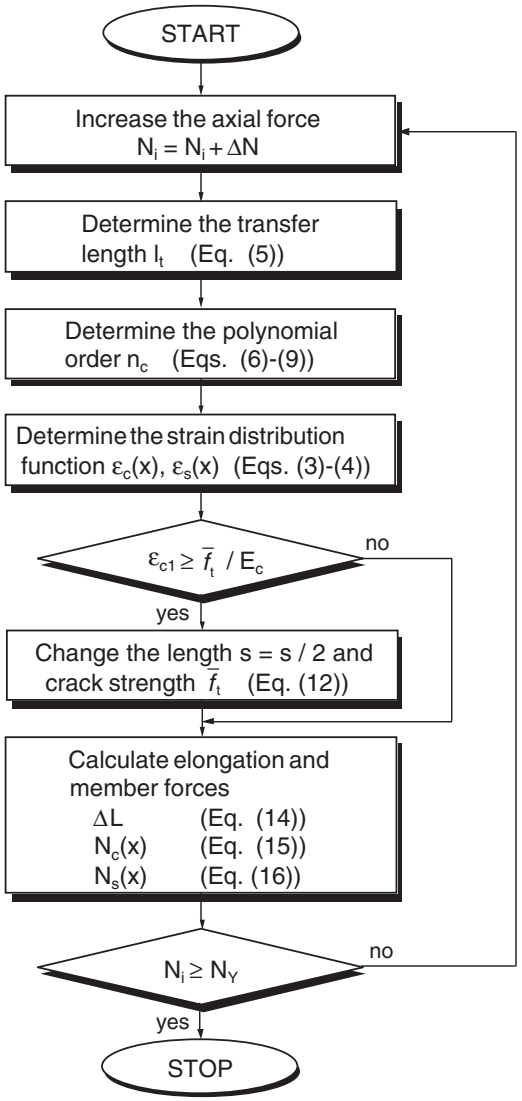

Fig. 4. Outline of solution algorithm.

constitutive relationships of cracked concrete and reinforcing steel in there formulations [8,10], there has been a renewed interest in the characterization of the average stress–strain behavior of tension members. Even though its calculation procedure is simple and effective [11], the direct application of an approach that uses the effective area of concrete, as in the ACI 224, may be inappropriate for determining the tension stiffening effect in the average stress–strain relation. This method is not suitable because of its relatively weak theoretical background and the difficulty involved in constructing the material matrix.

Accordingly, the model introduced in this paper is based on an average strain concept with assumed strain distribution function because it has greater ease of application and convenience in terms of the axial problem. The following basic assumptions are adopted: (1) at the fully cracked state (STATE II in Fig. 1), the reinforcing steel maintains the load carrying capacity for both tensile and compressive forces while the concrete resists the compressive force only; (2) at the uncracked state (STATE I in Fig. 1), the reinforcing steel and concrete can resist both the applied tensile and compressive forces; and (3) at the post-cracking state, the stiffness of an RC member is gradually reduced due to progressive cracking.

The validity of the proposed approach is established by comparing the analytical predictions for RC tension members with results from experiments and from previous analytical studies. Moreover, numerical analyses for the cracking behavior of two typical RC walls tested by Kheder [12] are conducted to verify the validity of the proposed analytical model.

2. Bond–slip behavior of tension member

A section of an RC member subjected to uniaxial tension is shown in Fig. 2. When the axial load N is applied, from the basic assumptions adopted, the far ends represent the fully cracked state with a steel strain of ε_{s2} (see Fig. 1). In addition, the tensile force N is transferred from the steel bar to the concrete by bond stress, and the value of the bond stress is zero at the inner end of the transfer length l_t. This means that there is no bond–slip within the central region bounded by the transfer length. Moreover, it can be assumed that the strains in steel and concrete are equal to each other at $x=l_t$, and that the strain value corresponds to ε_{s1} (see Fig. 1).

From the strain distribution, the local slip $w(x)$ can be defined as the total difference in elongations between the reinforcement and the concrete matrix measured over the length between the distance x from a crack face and the center of the segment ($x=s/2$). That is

$$w(x) = \int_x^{s/2} (\varepsilon_s(x) - \varepsilon_c(x))\mathrm{d}x \tag{1}$$

where s is the length between two adjacent cracks, which is equivalent to the crack spacing, and $\varepsilon_s(x)$ and $\varepsilon_c(x)$ are the strain distributions of steel and concrete, respectively.

On the basis of the force equilibrium and the relation of Eq. (1), the following familiar governing differential equation for the bond–slip can be obtained [13].

$$\frac{\mathrm{d}^2 w(x)}{\mathrm{d}x^2} - \frac{(1+n\rho)\Sigma_o}{E_s A_s} f_b(x) = 0 \tag{2}$$

where $n=E_s/E_c$, the steel ratio $\rho=A_s/A_c$, Σ_o is the perimeter of the steel bar, f_b is the bond stress at the steel interface, and E_s and A_s are Young's modulus and the sectional area of steel, respectively.

The general solution of Eq. (2) is obtained in previous studies by applying the boundary conditions at the crack face and at the center of the cracked region based on an assumed bond stress distribution [11,13,14]. After obtaining the general solution for the bond–slip, the strain distributions of steel and concrete and the corresponding bond stress along the steel axis are successively calculated using the force equilibrium and the compatibility condition at an arbitrary location [11,13,14]. However, this approach has some limitations in estimating the cracking behavior of RC axial members

Table 1
Material properties used in applications

Specimens	E_c (GPa)	E_s (GPa)	f_t (MPa)	d_s (mm)
1	24.8	199.9	1.38	25.4
2	23.8	199.9	2.12	25.4
3	30.1	195.8	2.34	25.4

1 mm=0.0394 in., 1 MPa=0.145 ksi.

Table 2
Comparison of crack loads for Specimen 1 (unit: kN)

No. of cracks	Gerstle [15]	Chan [18]	This study
1	30.1	30.1	30.1
2	30.3	30.6	30.6
4	32.2	34.1	34.8
8	56.5	49.8	50.7

1 kN=0.225 kips.

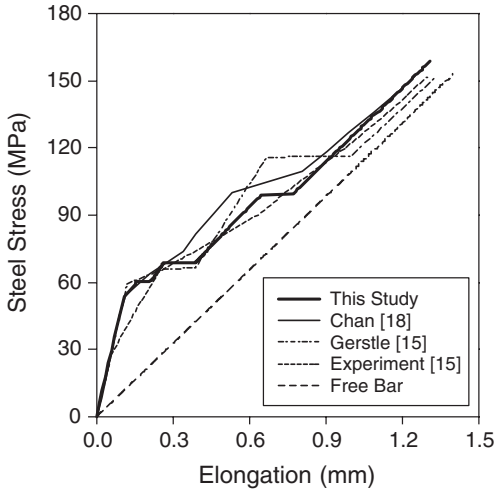

Fig. 5. Steel stress-elongation relation of Specimen 1 (1 mm=0.0394 in., 1 MPa=0.145 ksi).

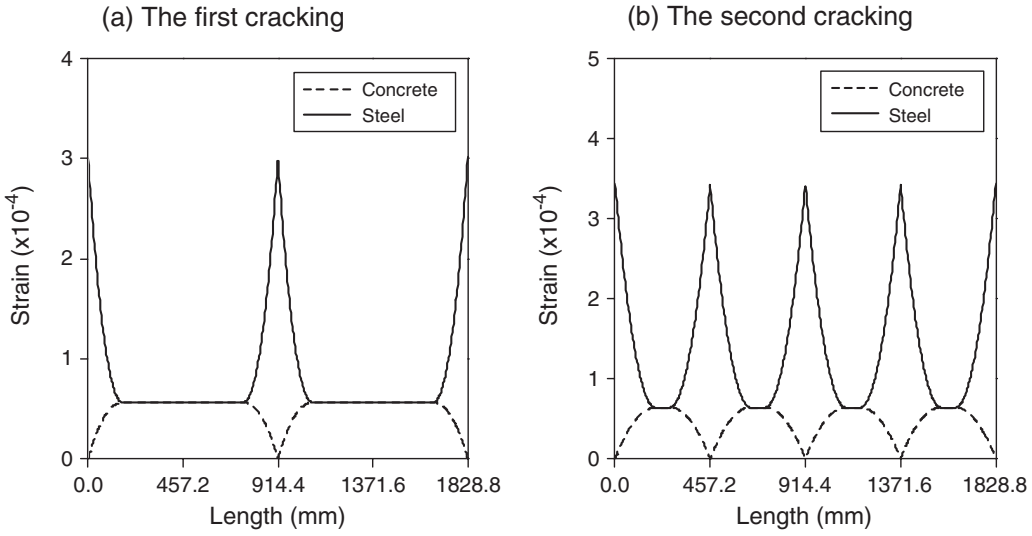

Fig. 6. Typical steel strain distribution according to cracks (1 mm=0.0394 in.).

because it requires a series of complex integration and derivation procedures and the calculated location representing the maximum bond stress value is not coincident with that obtained from experimental studies. To solve these limitations, an analytical approach on the basis of the assumed strain distribution function of concrete is introduced in this paper.

3. Proposed analytical approach

3.1. Strain distribution functions

When the applied axial load N_1 is relatively small, the small strains in steel and concrete maintain a uniform distribution with $\varepsilon_{s1}=N_1/(A_sE_s+A_cE_c)$ along the length. As the axial load N_2 gradually increases, the strains in steel and concrete represent different distributions in the region from the crack face to the inner end of the transfer length (see Fig. 3). Moreover, from the basic assumptions adopted, the steel strain ε_{s2} at the crack face and ε_{s1} at the center of the segment become $\varepsilon_{s2}=N_2/A_sE_s$ and $\varepsilon_{s1}=N_2/(A_sE_s+A_cE_c)$, respectively.

From Fig. 3, the concrete strain distribution $\varepsilon_c(x)$ is approximated with a general nth order polynomial function, and the steel strain distribution $\varepsilon_s(x)$ can also be expressed in terms of the concrete strain distribution function from the force equilibrium of $N_2=\varepsilon_{s2}A_sE_s=\varepsilon_{s1}(A_sE_s+A_cE_c)$ and the relation of $\varepsilon_{s1}=\varepsilon_{c1}$. The strain distributions lead to

$$\varepsilon_c(x)=\varepsilon_{s1}\left(1-\left(1-\frac{x}{l_t}\right)^{n_c}\right) \qquad 0\le x\le l_t \tag{3}$$

$$\varepsilon_s(x)=\varepsilon_{s2}-\frac{1}{n\rho}\varepsilon_c(x)$$

$$\varepsilon_c(x)=\varepsilon_s(x)=\varepsilon_{s1} \qquad l_t\le x\le s/2 \tag{4}$$

where the area parameter $n\rho$ is in the range of 0.02–0.5 [15]. Moreover, the transfer length l_t can be determined by the

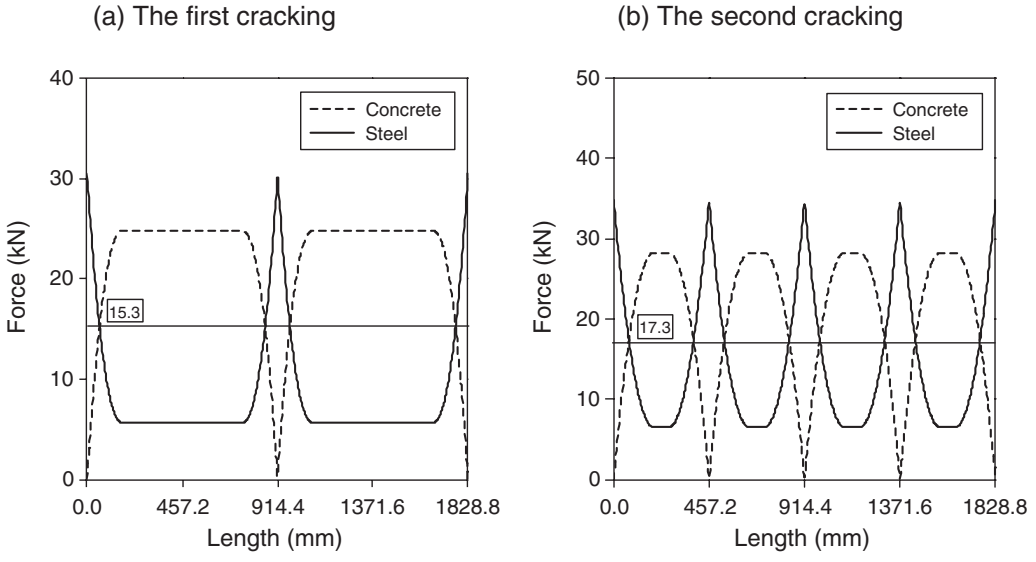

Fig. 7. Typical distribution of forces carried by steel and concrete (1 mm=0.0394 in., 1 kN=0.225 kips).

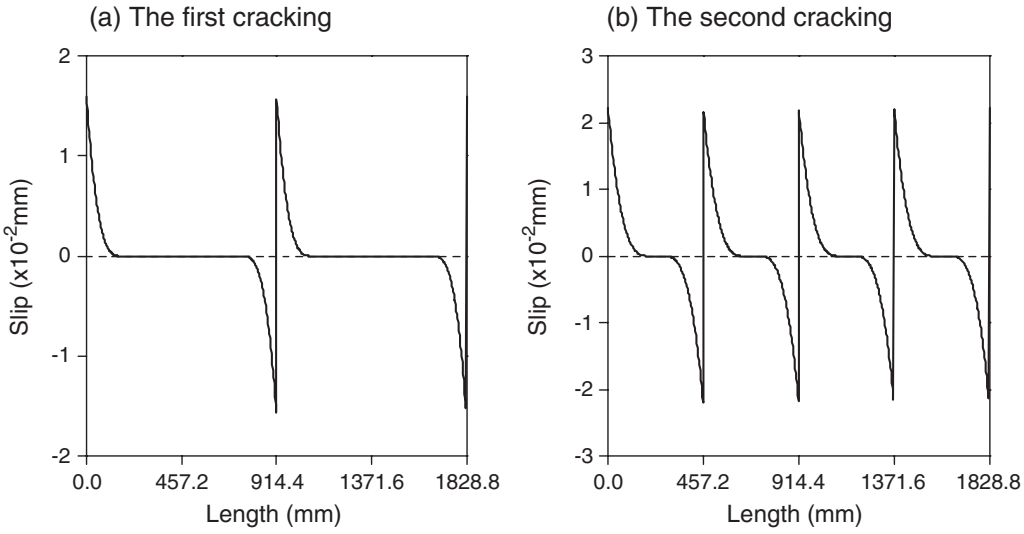

Fig. 8. Typical slip distribution at each cracking stage (1 mm=0.0394 in.).

following linear relationship proposed by Somayaji et al. [14] on the basis of extensive experimental data for the pull-out tests:

$$l_t = K_p \frac{N_c}{\Sigma_o} \tag{5}$$

where N_c is the transfer load equal to $N_c = A_c E_c \varepsilon_{s1} = N/(1+n\rho)$, and K_p is a constant determined from the pull-out test. The experimental study by Mirza et al. [16] indicates that the value of K_p is in the range of 0.20–0.55 mm^2/N (1/714–1/266 in.^{2}/lb). Therefore, an average value of 0.38 mm^2/N (1/385 in.^{2}/lb) is used in this paper.

The strain distribution of the reinforcing bar changes from the uniform distribution ε_{s1} along the segment before cracking to the assumed polynomial distribution with the strain ε_{s2} at the crack face and ε_{s1} at the inner end of the transfer length after cracking (see Fig. 3). Based on energy conservation just before and after cracking at the same axial load N, the assumed polynomial order n_c can be determined because all the internal strain energy components can be represented in terms of the concrete strain with the assumed polynomial order n_c, while there is no additional external work by the axial load N just at cracking. The strain difference of steel $\varepsilon_s(x) - \varepsilon_{s1}$ represents an increase of the strain energy at the reinforcing steel, ΔU_s, and that of concrete, ΔU_c corresponds to a decrease of the strain energy at the concrete, $\varepsilon_{s1} - \varepsilon_c(x)$. Moreover, the difference between ΔU_s and ΔU_c represents the energy loss caused by the bond–slip, ΔU_b. Therefore, the energy conservation can be written as

$$\Delta U_s - \Delta U_c = \Delta U_b \tag{6}$$

where

$$\Delta U_s = A_s E_s \int_0^{l_t} (\varepsilon_s(x) - \varepsilon_{s1})^2 dx = \frac{A_s E_s \varepsilon_{s1}^2 l_t}{n^2 \rho^2 (2n_c + 1)} \tag{7}$$

$$\Delta U_c = A_c E_c \int_0^{l_t} (\varepsilon_{s1} - \varepsilon_c(x))^2 dx = \frac{A_c E_c \varepsilon_{s1}^2 l_t}{2n_c + 1} \tag{8}$$

$$\Delta U_b = \int_0^{l_t} \tau_b(x) \Sigma_o w(x) dx = \frac{\Sigma_o \tau_{max}}{w_1^\alpha} \frac{\varepsilon_{s2}^{(1+\alpha)} l_t^{(1+\alpha)} l_t}{(n_c+1)^{(1+\alpha)}((n_c+1)(1+\alpha)+1)}. \tag{9}$$

While calculating the bond energy variation ΔU_b, the relation of Eq. (1) and the following nonlinear bond stress–slip relation [5] are used:

$$\tau_b = \tau_{max}(w/w_1)^\alpha \tag{10}$$

where τ_{max} is the maximum bond stress of concrete, and w_1 and α have the values of 1 mm and 0.4, respectively, when

Table 3
Comparison of steel stress at crack loads for Specimen 2 (unit: MPa)

No. of cracks	Khouzam [20]	Chan [18]	This study
1	113.8	100.0	106.2
2	131.0	144.8	159.3

1 MPa=0.145 ksi.

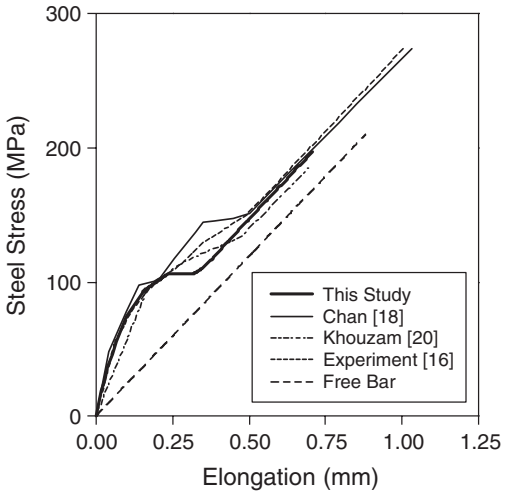

Fig. 9. Steel stress-elongation relation of Specimen 2 (1 mm=0.0394 in., 1 MPa=0.145 ksi).

Table 4
Comparison of steel stress at crack loads for Specimen 3 (unit: MPa)

Dimensions	No. of cracks	Chan [18]	This study
50.8 mm × 50.8 mm	1	20.7	24.8
	2	24.8	25.5
	4	29.0	28.3
101.6 mm × 101.6 mm	1	66.2	73.8
	2	99.3	115.1
152.4 mm × 152.4 mm	1	194.4	224.8

1 mm = 0.0394 in., 1 MPa = 0.145 ksi.

very good bonding conditions are maintained in a confined concrete [5].

As shown in Eqs. (7)–(9), all the strain energy variations are expressed with the assumed polynomial order n_c. Consequently, the order n_c can be determined through successive iterations until Eq. (6) is satisfied. After the first cracking, however, there is no guarantee that a direct application of Eq. (6) will give a lower order n_c as subsequent cracks occur. To prevent unexpected calculations of the order n_c, the following lower boundary for n_c is defined in this paper.

As shown in Fig. 1, the tension stiffening effect corresponding to an applied axial load N_m can be defined with a strain difference between ε_{s2} and ε_{sm} ($\varepsilon_{TS}=\varepsilon_{s2}-\varepsilon_{sm}$). Moreover, the average steel strain can be represented by $\varepsilon_{sm}=\varepsilon_{s2}-1/n\rho\cdot\varepsilon_{cm}$ from Eq. (3), and the average concrete strain can also be expressed by $\varepsilon_{cm}=n_c/(n_c+1)\cdot\varepsilon_{s1}$ within the transfer length range when the strain distribution of $\varepsilon_c(x)$ is defined with a n_c-th order polynomial function. Accordingly, the strain difference corresponding to the tension stiffening effect can finally be expressed by $\varepsilon_{TS}=\varepsilon_{s2}-\varepsilon_{sm}=\varepsilon_{s2}-(\varepsilon_{s2}-1/n\rho\cdot\varepsilon_{cm})=1/n\rho\cdot\varepsilon_{cm}=1/n\rho\cdot n_c/(n_c+1)\cdot\varepsilon_{s1}$. On the other hand, the strain difference ε_{TS} must be gradually decreased as the applied axial load N increases. Namely, the strain difference at the first cracking (ε_{TS}^{cr}) must always be greater than that at an arbitrary axial load N(ε_{TS}^{N}), and this condition induces the following inequality condition of

$$\left(\frac{n_c}{n_c+1}\right)^{N}\le\left(\frac{n_c}{n_c+1}\right)^{cr}\frac{\varepsilon_{s1}^{cr}}{\varepsilon_{s1}^{N}}. \tag{11}$$

Consequently, successive iterations of Eq. (6) must be continued in the range of n_c, which satisfies the inequality condition of Eq. (11).

3.2. Crack strength

Due to the actual non-uniform distribution of concrete stress in the transverse and longitudinal directions in an RC tension member, many researchers [14,17] have observed that the crack strength $\bar{f}_t$ of an RC member is different from the tensile strength f_t of plain concrete. The latter is a physical characteristic for plain concrete while the former is defined here as the stress level of concrete at which cracking takes place in an RC member. The crack strength of an RC member increases with a decrease of the ratio of length of segment to cross-sectional area and with an increase of the strain gradient in the transverse or longitudinal directions. To consider the change in the tensile strength of concrete according to the loading history, Chan et al. [18] introduced the following relation:

$$\bar{f}_t=\alpha f_t\left(\frac{\sigma_{c,max}}{\sigma_{c,ave}}\right)^{\beta} \tag{12}$$

where $\sigma_{c,max}$ is the maximum stress of concrete and $\sigma_{c,ave}$ is the average stress of concrete along the length. α and β are material constants to be determined from the test data and are in the range of 0.86–0.98 and 0.8–0.9, respectively [18]. The average values of $\alpha=0.92$ and $\beta=0.85$ are used in this paper. However, α and β may depend on the size of specimens. When a large specimen is used, the average stress of concrete may give a relatively small value. Nevertheless, the existing literature does not specify any criteria for considering the variation of tensile strength due to specimen length. If logical and specific criteria for this determination are established by experimental studies and analytical approaches, improved numerical results can be expected.

In this paper, the tensile strength of plain concrete is used as the crack strength until the first crack forms at the center of the specimen. The crack strength as calculated by Eq. (12) is applied when a subsequent crack forms, in order to reflect an increase of the crack strength with a decrease in the length of the segment. Moreover, the maximum stress of concrete $\sigma_{c,max}$ can be calculated by $\varepsilon_{s1}E_c$ (see Fig. 3), and for the average stress of concrete $\sigma_{c,ave}=\varepsilon_{cm}E_c$, the average strain of concrete ε_{cm} may be calculated by

$$\varepsilon_{cm}=\frac{2}{s}\int_0^{s/2}\varepsilon_c(x)dx. \tag{13}$$

Since the number of cracks will increase with an increase of the applied axial force N, the crack spacing s will

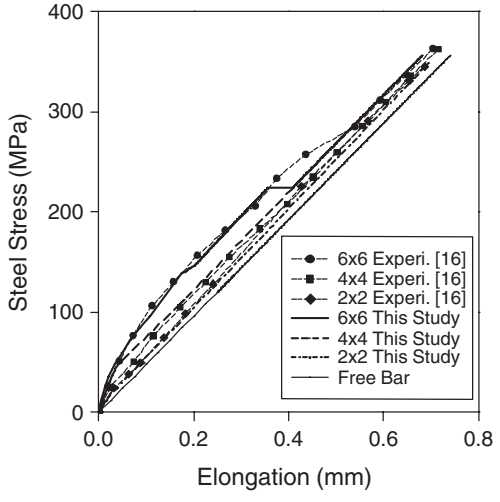

Fig. 10. Steel stress-elongation relation of Specimen 3 (1 mm = 0.0394 in., 1 MPa = 0.145 ksi).

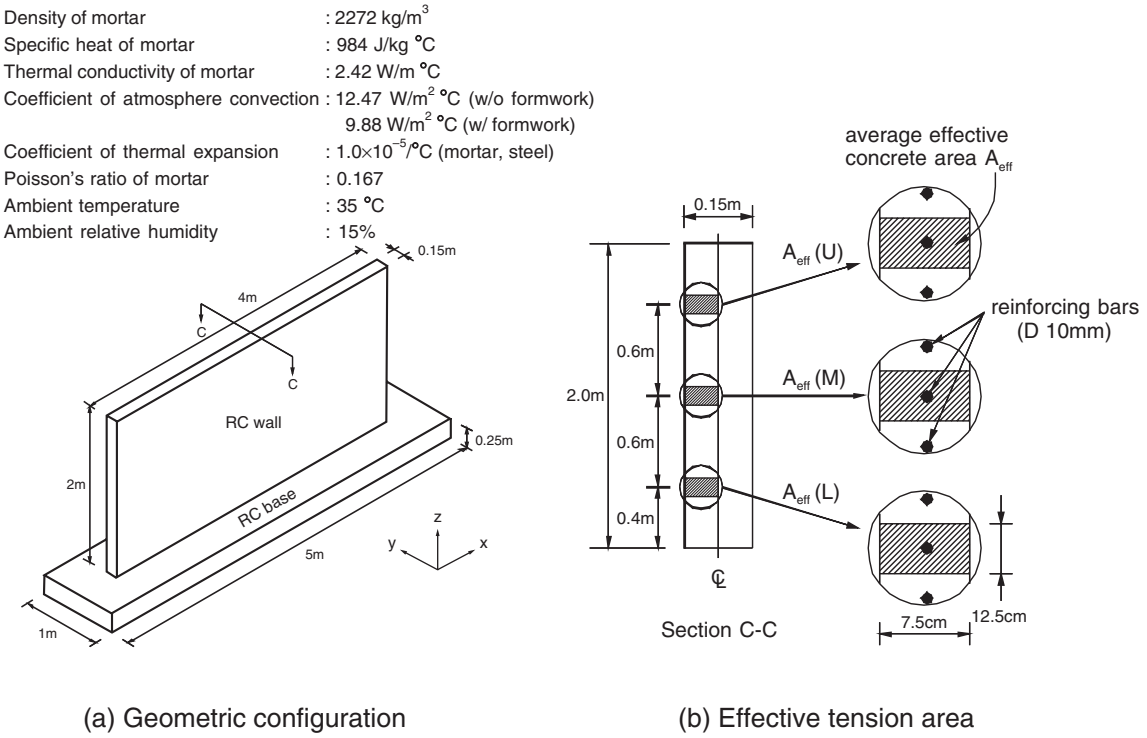

Fig. 11. Specimen 1E2.

decrease, which will be accompanied by a decrease of the average strain of concrete. Consequently, a decrease in the average stress of concrete $\sigma_{c,ave}$ and an increase in crack strength $\overline{f}_t$ will emerge as the number of cracks increases.

After determination of the crack spacing s and of the corresponding steel stress f_s using the introduced analytical approach, the crack width can also be predicted by using the Gergely-Lutz equation adopted in the ACI 207 [19]. Many previous studies [19] have observed that the crack spacing in unreinforced concrete walls is one to two times the wall height, and that the crack spacing in base-restrained walls is determined by the combined effects of the restraining base and the horizontal steel reinforcement provided in the wall. Based on these observations, many crack spacing and width-predicting formulas have been proposed [1–4]. Therefore, to establish the validity of the proposed analytical model, we compare the numerical results predicted by the proposed analytical model with those predicted by other formulas [1–4] and with experimental data [12].

4. Solution procedure

For each load increment, successive numerical estimations of cracking behavior in an RC tension member are conducted from the determination of the assumed polynomial order n_c (see Eq. (3)) to the calculation of the crack strength (see Eq. (12)). These steps are presented in detail in the flow diagram of Fig. 4.

As previously mentioned, conventional approaches based on assumed bond stress distribution determine the slip distribution, which is the general solution of the governing differential equation (see Eq. (2)), and then a series of repeated complex integrations and derivations at each nodal point along the specimen must be performed to determine the deformation states of concrete and steel. Because an analytical approach based on assumed concrete strain distribution functions does not require these additional calculations, this type of approach is more effective than conventional bond stress approaches in predicting the cracking behavior of a tension member. In the proposed

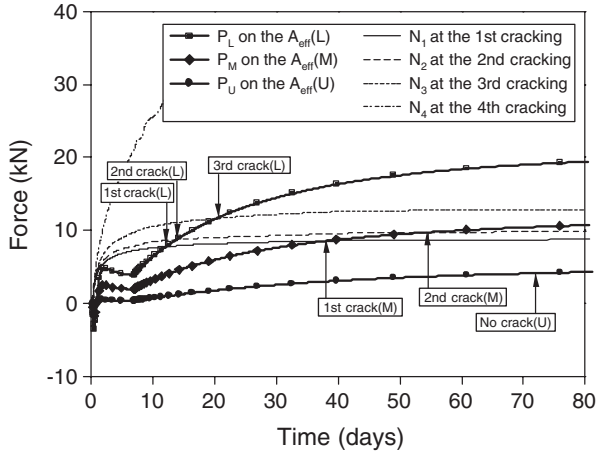

Fig. 12. Axial force distributions at specimen 1E2.

Table 5
Comparison of crack width w_{max} and crack space S

Crack comp.	Wall level	Hughes [1]	Stoffers [2]	Harrison [3]	Al Rawi et al. [4]	This study	Observed [12]
w_{max} (mm)	Upper	0.398	0.448	−0.024	–	–	–
	Middle	0.398	0.448	0.035	0.100	0.135	0.14
	Lower	0.398	0.339	0.112	0.280	0.245	0.25
S (m)		0.21–0.42	2.0–3.0	0.21–0.42	0.48–0.97	0.50	0.34–0.89

method, the deformation states of each material can be determined through the following calculation:

$$\Delta L = \int_0^L \varepsilon_s(x)\mathrm{d}x \tag{14}$$

$$N_c(x) = \varepsilon_c(x)E_cA_c \tag{15}$$

$$N_s(x) = \varepsilon_s(x)E_sA_s. \tag{16}$$

5. Experimental verification for RC tension members

In order to test the proposed approach, the cracking responses of tension members subjected to direct tensile force are analyzed. Three kinds of tension members are selected, and each specimen is modeled with elements measuring 25.4 mm (1 in.) length. The material properties of the test specimens are summarized in Table 1.

The first tension pull-out test specimen (Specimen 1) is a circular specimen with the following dimensions: the diameter of the concrete section, D, is 152.4 mm (6 in.), and the length of the specimen, L, is 1828.8 mm (72 in.). This specimen was previously tested and analyzed by Gerstle et al. [15] using a complex, large-scale computer program employing the fracture mechanics approach and the discrete crack model. It was also analyzed by Chan et al. [18] using assumed bond stress distribution.

The first crack forms at a load of 30.1 kN (6.77 kips), and subsequent cracks are formed as follows: two cracks form at a load of 30.6 kN (6.87 kips), four cracks at a load of 34.8 kN (7.83 kips), and eight cracks at a load of 50.7 kN (11.4 kips). The ultimate crack spacing reaches $s = 1828.8\ \mathrm{mm}/2^4 = 114.3$ mm (4.5 in.). As shown in Table 2, the crack loads obtained by the proposed method agree well with those obtained analytically by other researchers using other methods.

Comparisons of the experimental and analytical steel stress-elongation relation of the specimen are shown in Fig. 5. The prediction agrees well with the test results and with previous analytical results, and the proposed approach actually predicts the cracking behavior of Specimen 1 better through all the loading steps than previous methods. The slope of the steel stress-elongation relation converges to that of a free bar, and crack loads, corresponding to steel stresses of 59.3 MPa (8.6 ksi), 60.0 MPa (8.7 ksi), 68.3 MPa (9.9 ksi), and 100.0 MPa (14.5 ksi), accompany a relatively large elongation that is not proportional to the applied load. It seems to be caused by an immediate increase of bond–slip at each cracking.

After cracking, variation in the strain distribution of steel appears larger than that of concrete as the applied load increases. The steel strain has a maximum value at the crack face because at this location the steel alone must resist the applied load without the benefit of any additional tension stiffening from the concrete (see Fig. 6).

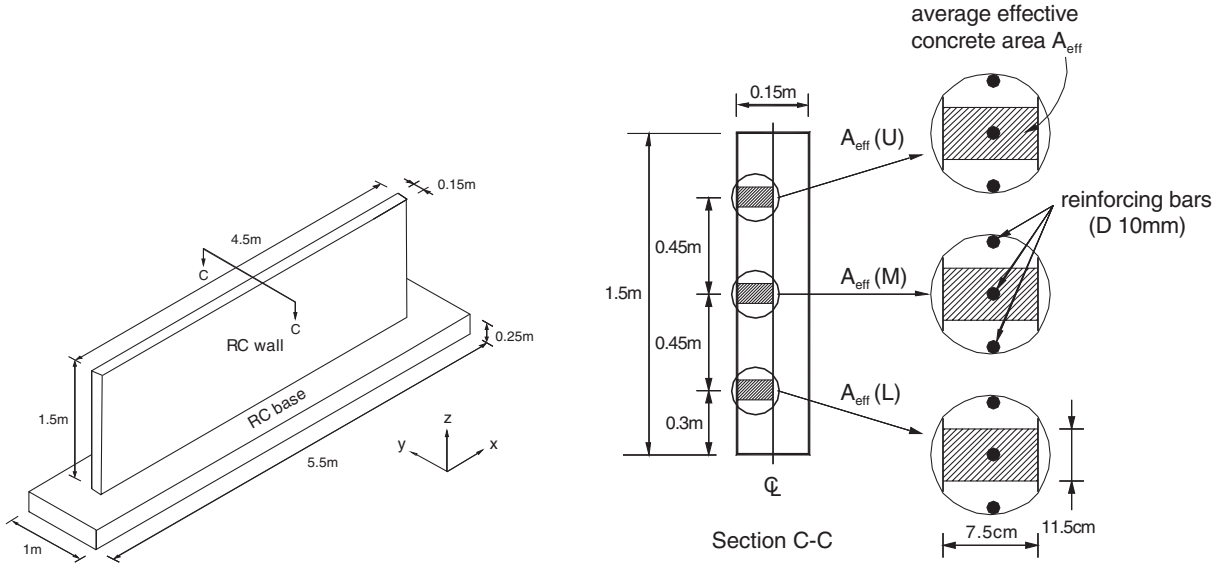

(a) Geometric configuration (b) Effective tension area

Fig. 13. Specimen 2E2.

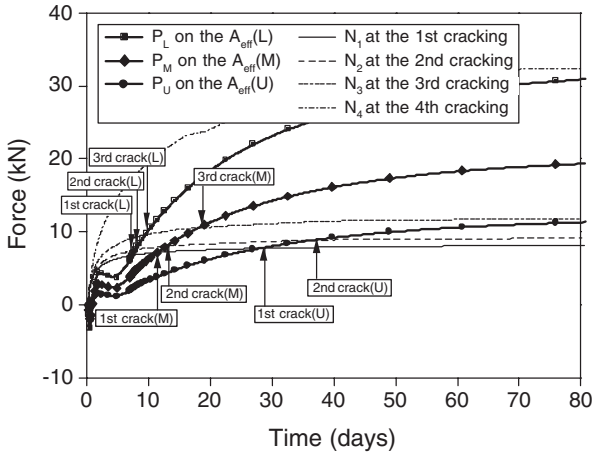

Fig. 14. Axial force distributions at specimen 2E2.

Fig. 7 illustrates the manner in which the axial load is shared between the concrete matrix and the reinforcing steel and shows how this load sharing is influenced by the formation of cracks. As shown in Fig. 7, the force carried by concrete gradually decreases as the number of cracks increases. Before the first cracking, the force carried by concrete reaches 72% of the applied axial force. However, at the fully cracked stage, the portion of the force carried by the concrete is reduced to just 5%. In addition, as the applied load increases, the crack spacing converges to the section width of the specimen with an increase of the total of all the transfer lengths and the bond–slips at the crack faces (see Fig. 8).

The second example (Specimen 2) is a rectangular tension member measuring 205.74 mm × 88.9 mm (8.1 in. × 3.5 in.). The specimen was previously analyzed by Khouzam [20] using the discrete crack model, and by Chan et al. [18] using assumed bond stress distribution. In this analysis, the first crack forms at a steel stress of 106.2 MPa (15.4 ksi) while subsequent cracks appear at a steel stress of 159.3 MPa (23.1 ksi). The ultimate crack spacing reaches 209.55 mm (8.25 in.), which is very close to the section width of the specimen. Comparisons of the analytical results with the test results and with the previous analytical results are shown in Table 3 and Fig. 9.

The third example (Specimen 3) is an analysis of four pull-out tests with different cross-sections previously tested by Mirza et al. [16] and analyzed by Chan et al. [18]. The specimen length is 406.4 mm (16 in.). All the obtained steel stresses at each cracking stage can be found in Table 4 and comparisons of the experimental and analytical steel stress-elongation relation of the specimen are shown in Fig. 10. The analytical results agree well with the experimental results.

The three preceding examples prove the validity of analyzing a reinforced concrete member under tensile loading using the proposed approach. The predictions of crack loads and crack spacing, and of the stress-elongation relation, are satisfactory when compared with test results and with previous numerical results.

6. Experimental verification for RC walls

To verify the applicability of the proposed analytical model to wall structures, two typical walls with different length (L) to height (H) ratios, tested by Kheder [12], are selected because the crack widths, spacings, and lengths in the walls strongly depend on the length to height ratio, L/H. After the casting of the concrete base, these walls were cast on an RC restraining base after an interval of 2 months to allow enough time for the volume change of the base to occur. A mortar mix with a 1:2 ratio of cement to sand and with a w/c ratio of 0.45 was used for casting the experimental walls. This mortar mix was used rather than a concrete mix in casting these walls because of its high and rapid drying shrinkage. The walls were reinforced with steel $\rho = 0.8\%$, were water-cured for a 7-day period, and were then exposed to the natural drying conditions of a hot and dry summer. More details related to the experimental walls can be found elsewhere [12], and the material properties used in the heat transfer and moisture diffusion analyses are listed in Fig. 11, as is the geometric configuration of the first specimen, 1E2.

As shown in Fig. 11(b), cracking analyses were conducted for three center sections located at 0.4 m, 1.0 m, and 1.6 m from the bottom face of wall, and A_{eff} (L), A_{eff} (M), and A_{eff} (U) represent the average effective concrete area at each location to calculate the average tensile force $P = \int_{A_{\text{eff}}} \sigma_x \mathrm{d}A$ from the heat transfer and moisture diffusion analyses compared in advance with the cracking load N from the crack model (see Fig. 2). Calculation of the number of cracks through a comparison of both force components of P and N makes it possible to calculate the average crack spacing and to determine the crack width by using the Gergely-Lutz equation [19]. Fig. 12 represents the variation of the two force components of P and N and shows, with time, that the possibilities for cracking at all sections do not coincide. The first crack occurred at a lower section after 12.3 days, and the second and third cracks occurred at 13.9 days and 20.3 days, respectively. In addition, the first and second cracks propagate to the middle section at 37.9 days and 54.3 days, respectively, but do not reach the upper section.

If it is assumed that, after cracking, all of the resisting force carried by the concrete is delivered to the reinforcing steel, then the steel stresses at the lower and middle sections after 60 days

Table 6
Comparison of crack width $w_{\max}$ and crack space S

Crack comp.	Wall level	Hughes [1]	Stoffers [2]	Harrison [3]	Al Rawi et al. [4]	This study	Observed [12]
$w_{\max}$ (mm)	Upper	0.419	0.448	0.043	0.110	0.139	0.13
	Middle	0.419	0.448	0.082	0.240	0.239	0.25
	Lower	0.419	0.272	0.138	0.360	0.383	0.40
S (m)		0.21–0.42	1.5–2.3	0.21–0.42	0.48–0.97	0.56	0.32–0.96

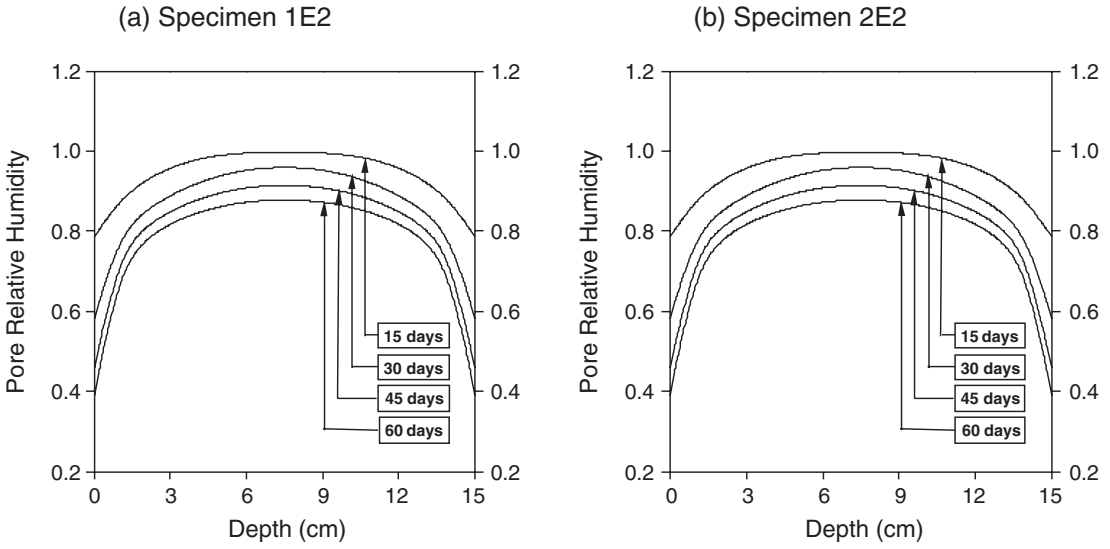

Fig. 15. Distribution of relative humidity across the depth.

become 236 MPa and 129 MPa, and the crack widths are calculated as 0.245 mm and 0.135 mm, respectively. Table 5 compares the maximum crack width and corresponding crack space obtained using the present method and the methods proposed by many previous researchers. From this comparison, it is clear that the results obtained using the proposed method are close to the observed experimental values. Unlike previous analytical models, excepting the one proposed by Rawi, the proposed method is able to predict the occurrence of the secondary crack and its propagation height in 1E2.

The second specimen, 2E2 [12], has $L/H=3$, and all the analysis conditions, except for the geometric configuration that is given in Fig. 13, are the same as those mentioned in the section covering the first specimen, 1E2. The obtained numerical result in Fig. 14 shows that the first cracking starts at 7.5 days from the lower section and subsequent cracks occur sequentially at very short time intervals (the second and third cracks occur at 8.0 days and 9.8 days, respectively). Unlike the previous specimen with $L/H=2$, the first and second cracks have the possibility for propagation to the upper section; their occurrence is estimated to be at 28.2 days and 37.1 days, respectively. Moreover, since the cracks occur three times at the bottom and middle sections along the length of $L=4.5$ m, the expected final crack spacing becomes 4.5 m/$2^3=0.56$ m. Maintaining the same assumptions as in the previous example, we estimate that after 60 days the

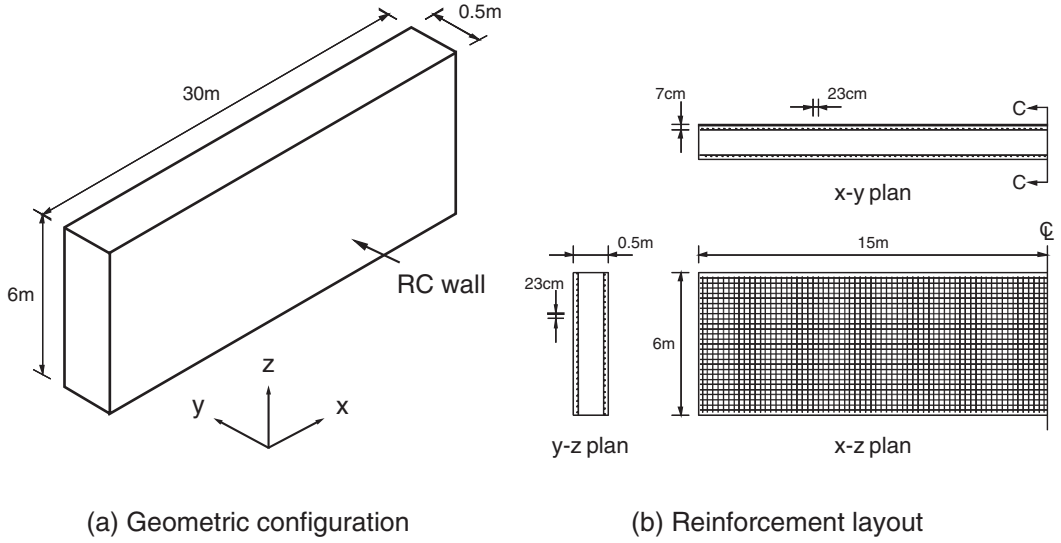

Fig. 16. Description of example structure.

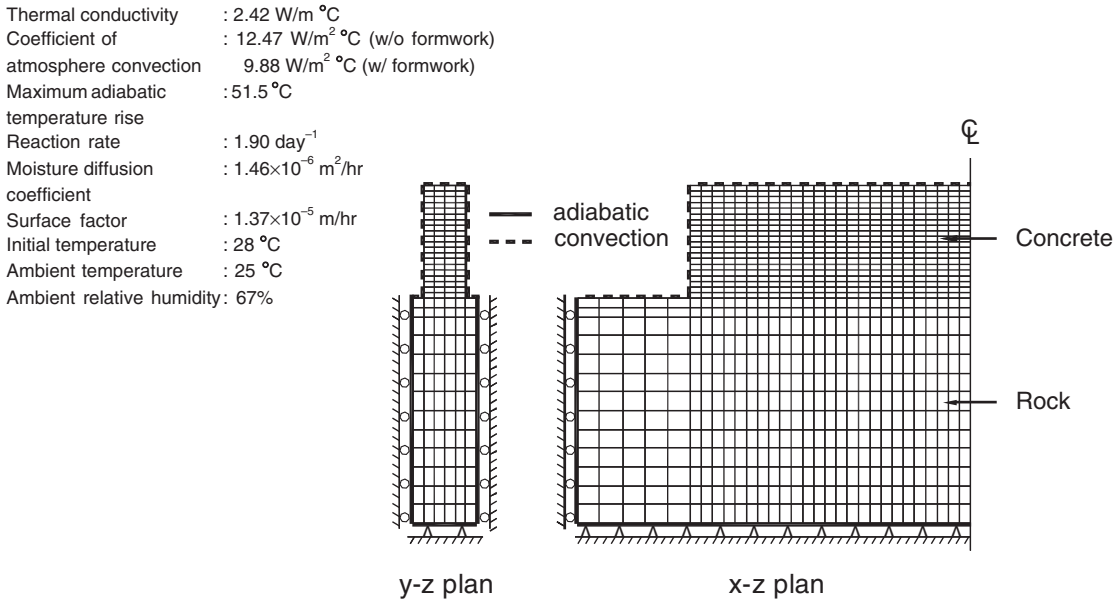

Fig. 17. Finite element discretization of example structure.

calculated steel stresses at the lower, middle, and upper sections will be 375 MPa, 234 MPa, and 136 MPa, respectively, and their corresponding crack widths will be 0.383 mm, 0.239 mm, and 0.139 mm, respectively. Table 6 gives the results with the experimental data and the other numerical results.

All the previous numerical models for analyzing the cracking of wall structures determined the crack width by considering only the wall's average volume change, calculated on the assumption that the shrinkage deformation would be identical at every location. However, it is found that this deformation is strongly affected by heat transfer and moisture diffusion. As shown in Fig. 15, the relative humidity across the depth of a wall is not constant but has a gradient even though the wall, at 15 cm, is relatively thin. This gradient causes a tensile stress on the surface because a larger restraint to the shrinkage deformation is developed on the surface. This means that the previous numerical models are limited because they fail to consider this stress variation across the depth; the discrepancy between the numerical prediction and the experimental data will increase as the thickness of the wall increases. In addition, since the previous numerical models were developed assuming that the wall's bottom face is fully restrained, a numerical analysis based on these models is somewhat limited because they do not consider a construction procedure in which the concreting of a wall is

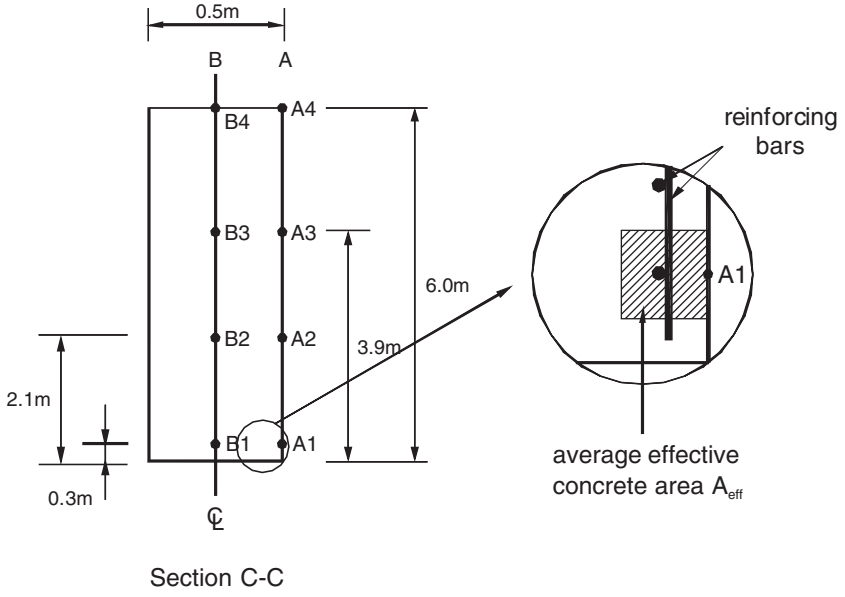

Fig. 18. Effective area A_{eff}.

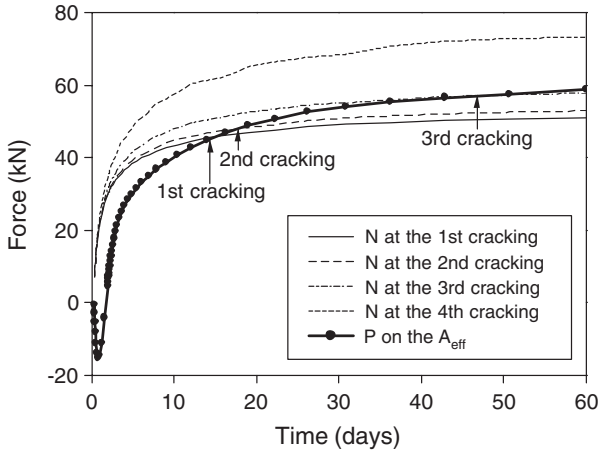

Fig. 19. Axial force distributions at A_{eff} (casting temperature T=28 °C).

performed on a concrete foundation that is not fully hardened and that shrinks continuously. Accordingly, since the proposed numerical model takes all of these factors into account, it can widely be used in numerical analyses and yields more accurate predictions concerning the cracking behavior of RC walls.

7. Application to RC walls

To evaluate how design parameters influence wall cracking, the geometry and cross-section dimensions of a sample structure, shown in Fig. 16, are selected because they represent the most common wall structure constructed in practice. A steel ratio of 0.5% in both directions is assumed. Taking advantage of the symmetry in geometry and the boundary condition, the finite element discretization in Fig. 17 represents only half of the structure in the x–z plan. A total of 4000 concrete elements and 4680 rock elements are used. The material properties used in the heat transfer and moisture diffusion analyses are given in Fig. 17, and the boundary conditions are the same as those used for the RC wall structure in the companion paper.

7.1. Quantitative evaluation of cracks

Since the maximum tensile stress due to shrinkage and hydration heat usually occurs on the surface of the center section C–C in Fig. 16(b), corresponding to point A1 in Fig. 18, quantitative cracking behavior such as the cracking space and the corresponding crack width is analyzed on the basis of the tensile stresses that occur around point A1. In particular, since determination of the crack width using the Gergely-Lutz equation requires the calculation of the average effective concrete area A_{eff}, the square area represented by the hatching lines in Fig. 18 is assumed in this paper.

The average tensile force P can be determined from $P = \int_{A_{eff}} \sigma_x dA$ and is compared, in advance, with the axial force N in Fig. 2, representing the cracking load in the introduced analytical approach. As shown in Fig. 19, which represents the variation with time of the two force components, P and N, the first crack in this example structure occurs at about 15 days after the concrete is poured, and the second and third cracks occur at 18 days and 47 days, respectively. The final crack spacing appears to be 3.75 m. In addition, if it is assumed that the axial force N is fully sustained by a reinforcing bar embedded after the cracking occurs, the tensile stress in the reinforcing bar reaches 201 MPa after the third cracks occur. Accordingly, the crack width, as determined using the ACI 207 [19], is 0.25 mm.

On the other hand, when the cracking behavior is estimated by Rawi's relation [4] proposed on the basis of the experimental data, the maximum and minimum crack spaces have values of 3.190 m and 1.595 m, respectively, and the crack width at the final cracking stage reaches 0.22 mm. These results show that the calculation of the axial force N using the introduced analytical model and the application of the ACI 207 to calculate the crack width give a reasonable result.

7.2. Effect of casting temperature

To investigate the cracking behavior according to the casting temperature of concrete, two different temperatures, 28 °C and

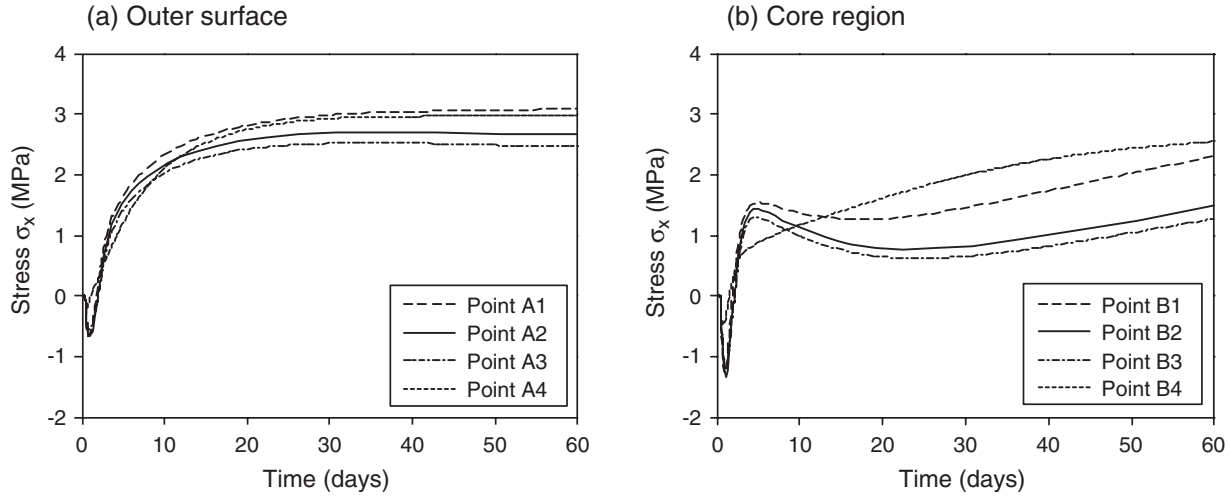

Fig. 20. Total stress when the casting temperature T=28 °C.

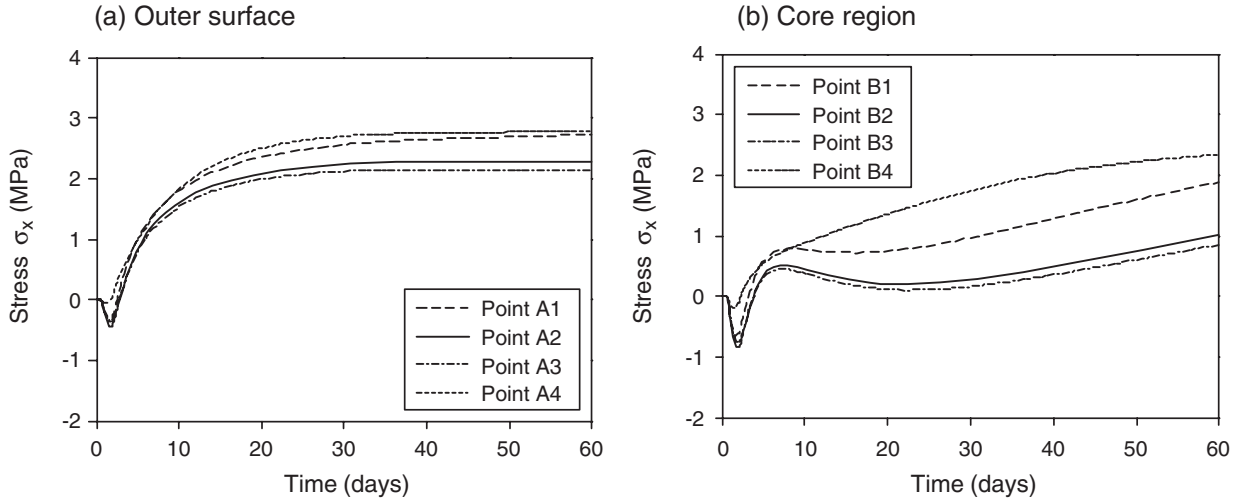

Fig. 21. Total stress when the casting temperature T=10 °C.

10 °C, are considered. The lower temperature of 10 °C is achieved through a pre-cooling method, and the maximum temperature rise and reaction rate influenced by the casting temperature are assumed to be 56.6 °C and 0.68 day^{-1}, respectively. The remaining assumed material properties and boundary conditions are the same as in the preceding example (see Fig. 17).

The variations of total stresses at the cross-section C–C (see Fig. 18) are shown in Figs. 20 and 21). As shown in these figures, the total stresses caused by the differential drying shrinkage and hydration heat represent a similar tendency regardless of differences in the casting temperature of concrete. However, the values themselves increase or decrease in proportion to the casting temperature because the stresses induced from the hydration heat decrease or increase depending on the casting temperature of concrete. On the other hand, the other stress components caused by the differential drying shrinkage maintain almost constant values regardless of the casting temperature. Since the example structure is relatively thin (t=50 cm), it is expected that the hydration heat will cause small stresses, and also that the severity of the total stresses will not be affected by the casting temperature of the concrete. Unexpectedly, however, Fig. 22 shows that a decrease of the casting temperature actually greatly contributes to the prevention of cracking in RC walls. That is, cracking in RC walls can be minimized by decreasing the casting temperature of the concrete, even in relatively thin RC walls.

7.3. Effect of casting length

As previously mentioned, a uniform distribution of vertical cracks develops in newly constructed RC walls along the entire span of the structure. These cracks are non-structural cracks and occur because of the restraint of volume change. Essentially, the restraints in an RC wall can be divided into two kinds of restraint: external and internal. Unlike internal restraint, which is generated as a result of a non-uniform distribution of movement across the wall thickness due to factors such as temperature and moisture, external restraint is generated by the foundation, the concrete of which is more mature and stable than the young concrete of the RC wall. Since a wall structure represents a high length to height ratio, which causes relatively large restraints, significant stresses can therefore result from external restraints. Accordingly, a parametric study for the effect

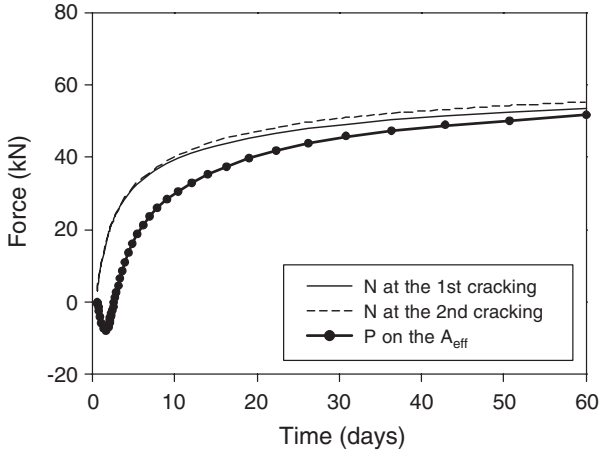

Fig. 22. Axial force distributions when the casting temperature T=10 °C.

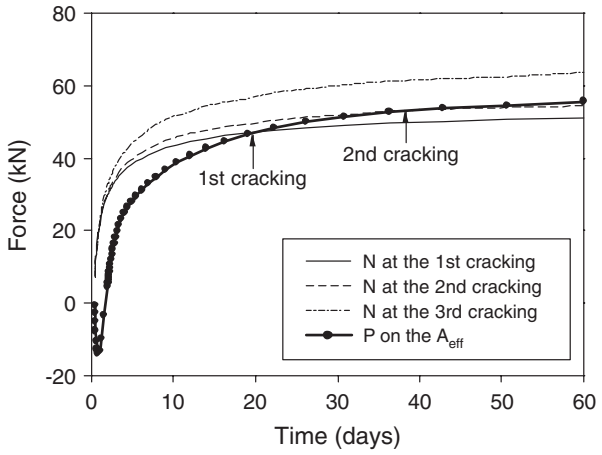

Fig. 23. Axial force distributions at A_{eff} when the casting length is 20 m.

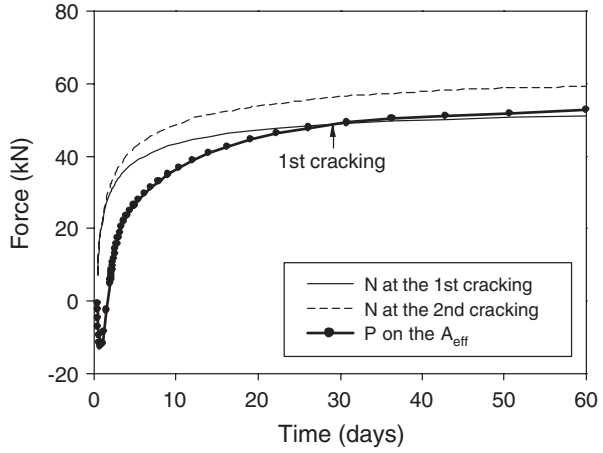

Fig. 24. Axial force distributions at A_{eff} when the casting length is 10 m.

of casting length of an RC wall is conducted in this paper by changing the casting lengths.

A decrease in the casting length accompanies the reduction of tensile stress. The relative rate of decrease is significantly larger in the upper region (see points A3 and B3 in Fig. 18) than in the lower region (see points A1 and B1 in Fig. 18), where the volume change is directly restrained because a larger variation to the relative restraint level appears at the upper region [19]. Figs. 23 and 24 compare the axial force distribution at A_{eff} in Fig. 18. When the casting length is 20 m, the first crack occurs at 20 days after casting and, at 38 days after casting, subsequent cracks develop and the crack spacing reaches 5 m. In contrast, Fig. 24 shows that the first crack occurs at 29 days after casting and that no more cracks occur. Even though the final crack spacings are the same for both cases, the crack widths as calculated by the ACI 207 differ because the average tensile force P decreases in proportion to the casting length. Comparison of the obtained results with those in Fig. 19, which represent the results for a casting length of 30 m, shows that closer cracks with a larger crack width occur as the casting length increases.

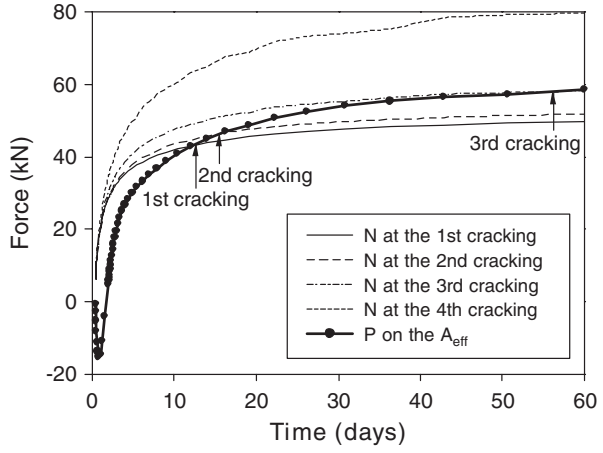

Fig. 25. Axial force distributions at A_{eff} when the steel ratio ρ=0.36%.

Table 7
Cracking behavior of an RC wall

Steel ratio (%)	Crack space (m)	Crack width (mm)
0.36	3.75	0.36
0.50	3.75	0.25
0.70	3.75	0.18

7.4. Effect of steel ratio

Properly placed reinforcement, used in adequate amounts, will prevent unsightly cracking. By distributing non-mechanical strains along the reinforcement through bond stresses, the cracks are distributed in such a way that a larger number of very fine cracks occur instead of a few wide cracks. The minimum amount and spacing of reinforcement to be used in walls are given in the ACI 318 [7]. Accordingly, a parametric study to determine the effect of reinforcing steel in the wall is conducted in this study.

Fig. 25 represents the axial force distributions at A_{eff} in Fig. 18. Since there are no changes in the temperature history and moisture distribution, a relatively minor influence on the stress variation is expected. Nevertheless, as mentioned with regard to the cracking behavior of an axial member, the steel ratio is still one of the most important influencing factors on the cracking behavior of concrete walls. As shown in Fig. 25, when the steel ratio decreases to 0.36%, the first crack occurs 12 days after pouring the concrete, and the second and third cracks occur at 16 days and 56 days, respectively. Specifically, the average crack space converges to 3.75 m, and the corresponding crack width by the ACI 207 is calculated as 0.36 mm. A comparison of the numerical results obtained with those presented in Fig. 19 shows that a decrease of the steel ratio results in an increase of the crack width and a reduction of the cracking time.

Similar analyses have been conducted for RC walls with steel ratios of 0.36%, 0.50% and 0.70%, and the obtained results are compared in Table 7. As shown in this table, the crack width gradually reduces from 0.36 mm to 0.18 mm as the steel ratio increases from 0.36% to 0.70%. The ACI 207 introduces a guide for the calculation of the steel ratio to maintain crack width within the allowable limit. For example, if the crack width needs to be maintained under 0.23 mm for a 30-m long RC wall, the steel ratio for the temperature and shrinkage must be greater than 0.62%. Table 7 suggests that the ACI 207 provides a reasonable guide to control cracking in RC walls and that it can be used with the proposed analytical model to evaluate the cracking of RC walls at an arbitrary time.

8. Conclusions

In this paper, an improved analytical model for a quantitative assessment of non-structural cracking in an RC wall is proposed. Firstly, to quantitatively calculate the cracking potential, an analytical model that can estimate the post-cracking behavior in an RC tension member is developed. Instead of using the assumed bond stress distribution, the concrete strain distribution with an nth order polynomial function is assumed and the polynomial order is determined

on the basis of energy equilibrium just before and after cracking. By adopting both the approach introduced in the companion paper as well as the one proposed in this paper, an improved analysis of the cracking behavior in RC walls can be performed.

Correlation studies between analytical and experimental results and the associated parametric studies for RC walls lead to the following conclusions: (1) in a tension member, the crack spacing converges to the section width of a specimen as the applied load increases; (2) the crack strength gradually increases as the number of cracks increases; (3) in an RC wall, the concrete temperature at casting greatly affects cracking and needs to be kept as low as possible; (4) closer cracks with a larger crack width occur as the casting length increases; (5) a decrease of the steel ratio results in wide cracks that appear relatively quickly.

Since the cracking of concrete depends on many design parameters, including the cement content, the slump, and the ratio of sand to aggregate, and also is influenced by the construction conditions discussed in this paper, the analytical model introduced in this paper can be effectively used to estimate the cracking potential. This is possible because this model takes changes in design parameters, as mentioned above, into consideration while calculating the stress caused by hydration heat and drying shrinkage of concrete. However, to reach a more precise approach for conducting a quantitative analysis for the cracking, extensive studies for reliability assessment, including more correlation studies between analytical and experimental results, still need to be done.

Acknowledgements

The authors would like to thank the Infra-Structures Assessment Research Center (ISARC) funded by Korea Ministry of Construction and Transportation (MOCT) for financial support.

References

[1] B.P. Hughes, Controlling shrinkage and thermal cracking, Concrete (London) 6 (5) (1972) 34–42.
[2] H. Stoffers, Cracking due to shrinkage and temperature variation in walls, Heron 23 (3) (1978) 5–68.
[3] T.A. Harrison, Early Age Thermal Crack Control in Concrete, CIRIA Rep. No. 91, Construction Industry Research and Information Association, London, 1981, 48 pp.
[4] R.S. Al Rawi, G.F. Kheder, Control of cracking due to volume change in base-restrained concrete members, ACI Struct. J. 87 (4) (1990) 397–405.
[5] Comite Euro-International du Beton, CEB-FIP Model Code 1990: Design Code, Thomas Telford, London, 1993.
[6] ACI Committee 224, Cracking of Concrete Members in Direct Tension (ACI 224.2R-92), ACI Manual of Concrete Practice, American Concrete Institute, Detroit, 1992.
[7] ACI Committee 318, Building Code Requirements for Structural Concrete and Commentary (ACI 318-02, ACI 318R-02), ACI Manual of Concrete Practice, American Concrete Institute, Detroit, 2001.
[8] F.J. Vecchio, M.P. Collins, Modified compression-field theory for reinforced concrete elements subjected to shear, J. Am. Concr. Inst. 83 (2) (1986) 219–231.
[9] T.T.C. Hsu, Softened truss model theory for shear and torsion, ACI Struct. J. 85 (6) (1988) 624–635.
[10] F.J. Vecchio, Disturbed stress field model for reinforced concrete: formulation, J. Struct. Eng.-ASCE 126 (9) (2000) 1070–1077.
[11] S. Yang, J. Chen, Bond–slip and crack width calculations of tension members, ACI Struct. J. 85 (4) (1988) 414–422.
[12] G.F. Kheder, A new look at the control of volume change cracking of base restrained concrete walls, ACI Struct. J. 94 (3) (1997) 262–271.
[13] A.K. Gupta, S.R. Maestrini, Tension-stiffness model for reinforced concrete bars, J. Struct. Eng.-ASCE 116 (3) (1990) 769–790.
[14] S. Somayaji, S.P. Shah, Bond stress versus slip relationship and cracking response of tension members, J. Am. Concr. Inst. 78 (3) (1981) 217–225.
[15] W. Gerstle, A.R. Ingraffera, P. Gergely, Tension stiffening: a fracture mechanics approach, Bond in Concrete, Applied Science Publishers, London, 1978.
[16] S.M. Mirza, J. Houde, Study of bond stress-slip relationships in reinforced concrete, J. Am. Concr. Inst. 76 (1) (1979) 19–46.
[17] J.S. Blackman, G.M. Smith, L.E. Young, Stress distribution affects ultimate tensile strength, J. Am. Concr. Inst. 55 (12) (1958) 679–684.
[18] H.C. Chan, Y.K. Cheung, Y.P. Huang, Crack analysis of reinforced concrete tension members, J. Struct. Eng.-ASCE 118 (8) (1992) 2118–2132.
[19] ACI Committee 207, Effect of Restraint, Volume Change, and Reinforcement on Cracking of Mass Concrete (ACI 207.2R-95), ACI Manual of Concrete Practice, American Concrete Institute, Detroit, 1995.
[20] M. Khouzam, A finite element investigation of reinforced concrete beams, State-of-the Art Report on Finite Element Analysis of Reinforced Concrete, ASCE, New York, 1982.